Smart Materials in Medicine 5 (2024) 127–139

Contents lists available at ScienceDirect

Smart Materials in Medicine

journal homepage: www.keaipublishing.com/en/journals/smart-materials-in-medicine/

Optimising degradation and mechanical performance of additively manufactured biodegradable Fe–Mn scaffolds using design strategies based on triply periodic minimal surfaces

Matthew S. Dargusch [a,*], Nicolas Soro [a], Ali Gokhan Demir [b], Jeffrey Venezuela [a], Qiang Sun [a], Yuan Wang [a], Abdalla Abdal-hay [c,d,e], Aya Q. Alali [c], Saso Ivanovski [c], Barbara Previtali [b], Damon Kent [a,f]

[a] Queensland Centre for Advanced Materials Processing and Manufacturing (AMPAM), School of Mechanical and Mining Engineering, Advanced Engineering Building, Bld 49, The University of Queensland, Staff House Rd, St Lucia, QLD, 4072, Australia
[b] Department of Mechanical Engineering, Politecnico di Milano, Via La Masa 1, 20156, Milan, Italy
[c] School of Dentistry, The University of Queensland, Herston Campus, 4072, Australia
[d] Department of Engineering Materials and Mechanical Design, Faculty of Engineering, South Valley University, Qena, 83523, Egypt
[e] Faculty of Industry and Energy Technology, Mechatronics Technology Program, New Cairo Technological University, New Cairo - Fifth Settlement, Cairo, 11835, Egypt
[f] School of Science, Technology and Engineering, University of the Sunshine Coast, Maroochydore BC, QLD, 4558, Australia

ARTICLE INFO

Keywords:
Selective laser melting
Additive manufacturing
Biodegradable materials
Iron and its alloys
Bone implants

ABSTRACT

Additively manufactured lattices based on triply periodic minimal surfaces (TPMS) have attracted significant research interest from the medical industry due to their good mechanical and biomorphic properties. However, most studies have focussed on permanent metallic implants, while very little work has been undertaken on manufacturing biodegradable metal lattices. In this study, the mechanical properties and *in vitro* corrosion of selective laser melted Fe–35%Mn lattices based on gyroid, diamond and Schwarz primitive unit-cells were comprehensively evaluated to investigate the relationships between lattice type and implant performance. The gyroid-based lattices were the most readily processable scaffold design for controllable porosity and matching the CAD design. Mechanical properties were influenced by lattice geometry and pore volume. The Schwarz lattices were stronger and stiffer than other designs with the 42% porosity scaffold exhibiting the highest combination of strength and ductility, while diamond and gyroid based scaffolds had lower strength and stiffness and were more plastically compliant. The corrosion behaviour was strongly influenced by porosity, and moderately influenced by geometry and geometry-porosity interaction. At 60% porosity, the diamond lattice displayed the highest degradation rate due to an inherently high surface area-to-volume ratio. The biodegradable Fe–35Mn porous scaffolds showed a good cytocompatibility to primary human osteoblasts cells. Additive manufacturing of biodegradable Fe–Mn alloys employing TPMS lattice designs is a viable approach to optimise and customise the mechanical properties and degradation response of resorbable implants toward specific clinical applications for hard tissue orthopaedic repair.

1. Introduction

Metal-based biomedical implants are extensively used in orthopaedic applications, such as in the fixation of bone fractures (fixation plates and screws) and bone tissue engineering (porous scaffolds) [1,2]. Inert metals, such as titanium and its alloys, stainless steels or cobalt-chromium alloys, have been used to fabricate orthopaedic implants due to their excellent biocompatibility, mechanical strength and high corrosion resistance [3]. Although permanent bone implants possess several advantages, they suffer from long-term health risks such as the potential to induce “stress shielding”, due to insufficient loading to maintain healthy bone tissue surrounding the implant caused by the implant material's higher relative stiffness, and possible toxicity from wear and element leaching [4]. Furthermore, for patients experiencing complications resulting from a permanent implant, removal of the implant requires expensive and painful secondary surgeries.

* Corresponding author.
E-mail address: m.dargusch@uq.edu.au (M.S. Dargusch).

https://doi.org/10.1016/j.smaim.2023.10.003
Received 3 August 2023; Received in revised form 11 October 2023; Accepted 12 October 2023
Available online 20 October 2023

Biodegradable/bioresorbable metallic implants can address some of these issues as they can provide sufficient mechanical support during healing to enable growth and repair of tissue and subsequently degrade in the physiological environment to be absorbed by the human body.

Currently, iron (Fe) [5], magnesium (Mg) [6,7] and zinc (Zn) [8] and their alloys are being explored as the most promising candidates for biodegradable metals. Among these, Fe-based alloys have advantages due to higher yield strength, ductility and hardness. Their mechanical properties are similar to 316L stainless steel, one of the most common permanent implant materials [9]. Such outstanding mechanical properties enable Fe-based implants to provide appropriate mechanical support when utilised to assist in healing large-volume bone defects. Additionally, Fe is well tolerated by the body, and toxicity is less likely than other metals such as Zn-based alloys because physiological Fe homeostasis is regulated by absorption only, rather than both absorption and gastrointestinal secretion and excretion as is the case for Zn [10]. Fe's excellent biocompatibility and physiological biodegradability have been verified by various *in vitro* tests [5,11,12]. This has also been explored in *in vivo* studies, with Peuster et al. [13] reporting that Fe implants do not cause local or systemic toxicity within the descending aorta of minipigs after 365 days. Dargusch *et al.* [14] also reported the absence of chronic systemic toxicity in rats after 12 weeks implantation with pure Fe. Nevertheless, the clinical application of biodegradable Fe is hindered by its intrinsically low degradation rate. For example, two long-term *in vivo* studies using pure Fe reported insignificant mass losses due to corrosion after one year of implantation [13,15]. Hence, for widespread adoption in clinical applications, it is necessary to find a suitable alloy/design that delivers the higher degradation rates required for implants to treat bone defects. A secondary consideration is the ferromagnetic nature of pure Fe which prohibits magnetic resonance imaging (MRI) of implants.

Alloying with Mn to form binary Fe–Mn alloys is an effective strategy to increase the degradation rate of pure Fe [5]. Hermawan et al. reported an eight-fold increase for *in vitro* corrosion of an Fe–35Mn alloy (1.26 mm $year^{-1}$) over pure Fe (0.16 mm $year^{-1}$) [16]. Dargusch et al. [17] showed the direct relationship between Mn concentration and corrosion rates in sintered Fe–Mn alloys (Fe–20Mn, Fe–30Mn and Fe–35Mn), which is also consistent with the observations by Hermawan et al. [9] for cold-rolled Fe–Mn alloys (Fe–20Mn, Fe–25Mn, Fe–30Mn and Fe–35Mn) and Kupkova et al. [18] for sintered Fe–Mn alloys (Fe–20Mn, Fe–30Mn and Fe–35Mn). Increased corrosion rates induced by introducing Mn to Fe can be attributed to the more active corrosion potential for Mn (−1.18 V) than Fe (−0.44 V), which consequently makes the system more susceptible to corrosion [19]. Furthermore, sufficient Mn additions (greater than 15 wt%) [5] promote the formation of γ-austenitic and ε-martensitic phases in place of the α-ferrite phase, with further increases in the proportion of γ-austenitic phase with increasing Mn. The presence of these dissimilar phases leads to microgalvanic corrosion that accelerates the overall bulk corrosion rate [2,9]. Mn alloying also induces antiferromagnetic behaviour in Fe due to the formation of the antiferromagnetic austenite and martensite phases [12], which makes the Fe–Mn alloys more compatible with MRI. Given these benefits, Fe–35Mn was selected for the current investigation as our previous work [17] has demonstrated that it exhibits the best combination of mechanical properties, MRI compatibility, suitable corrosion rates and excellent biocompatibility.

A porous structure is also favourable to boost the corrosion rates of Fe–Mn alloys due to increased surface area [20]. A substantial increase in corrosion rates was reported for the porous Fe–30Mn alloy (0.79 mm $year^{-1}$) compared to a nonporous, bulk Fe–30Mn alloy (0.02 mm $year^{-1}$) [21]. Additionally, open porosity allows transport of nutrients and oxygen which benefits bone formation and contributes to better fixation due to enhanced interfacial interaction with the surrounding tissues [22,23].

Additive manufacturing, particularly selective laser melting (SLM), is a proven technique for creating porous metallic scaffolds with controlled pore sizes. The process allows significant design flexibility facilitating the manufacture of metallic scaffolds incorporating intricate porous structures with mechanical properties tailored to specific implant applications [24].

Recently, porous metal scaffolds with lattice geometries based on Triply Periodic Minimal Surfaces (TPMS), including diamond, Schwarz and gyroid structures, have been proposed as outstanding candidates for use in bone scaffold applications. These structures exhibit a mean curvature of zero at any point, which alleviates potential geometric stress-concentrating features for these designs. Compared to more conventional lattices (e.g., cubic or dodecahedron), TPMS are also characterised by higher strength-to-weight and larger surface areas, which can enhance bio-integration [25,26]. There is a range of reports on the properties of TPMS lattices [27,28], particularly for metallic materials suitable for permanent implants such as titanium or stainless steel [29]. However, there are no reports on the impact of various TPMS lattice structures on the properties of Fe-based biodegradable alloys.

In a previous study the authors provided a comprehensive evaluation of Fe–Mn bone scaffolds based on a Schwarz primitive unit-cell manufactured by SLM [12,30], and *in vivo* tests revealed effective bone integration with the scaffolds and new bone formation within 4 weeks of implantation (Fig. 1). Despite these promising results, the initial study was limited to evaluation based on only one cell type. Additionally, this preliminary work also indicated the potential influence of unit cell type and porosity levels on degradation rates for the Fe–Mn scaffold. Consequently, the present study was conducted to more comprehensively understand the influence of different TPMS scaffold designs (i.e., diamond, Schwarz and gyroid) on mechanical properties, degradation rates and biological response for the porous Fe–35Mn alloy which can be used to develop optimised and customised solutions for patient and application specific treatments.

2. Experimental methods

2.1. Scaffold designs

The strut-based scaffold designs were based on gyroid, diamond and Schwarz primitive unit-cells (Fig. 2), which are all triply periodic minimal surface (TPMS) designs. The proposed unit-cell structures, reported for the Ti–6Al–4V alloy [31–33], show appropriate mechanical properties for use in hard tissue applications. The lack of discontinuity on their surfaces compared to conventional lattice designs (i.e., cubic, dodecahedron) presents advantages in terms of bone-ingrowth [34] and mechanical performance [35,36]. In contrast to sheet-based lattices, the strut-based (or skeletal) lattices applied in this work have improved pore connectivity due to their single cell domain [37]. These unit-cell geometries can be defined by mathematical functions [38], as follows:

$$F_{Gyroid}(x,y,z) = \cos(x)\sin(y) + \cos(y)\sin(z) + \cos(z)\sin(x) + K \quad \text{(Eq. 1)}$$

$$F_{Diamond}(x,y,z) = \sin(x)\sin(y)\sin(z) + \sin(x)\cos(y)\cos(z) + \cos(x)\sin(y)\cos(z) + \cos(x)\cos(y)\sin(z) + K \quad \text{(Eq. 2)}$$

$$F_{Schwarz\ p.}(x,y,z) = \cos(x) + \cos(y) + \cos(z) + K \quad \text{(Eq. 3)}$$

where K is an offset controlling the relative density (and corresponding level of porosity) which varies according to the different unit cell types as well as the required density. The values of K used in this work were based on the those reported by I. Maskery et al. [39] and are presented in Table 1. In this work, the porosity referred to is the designed and interconnected macro porosity within the lattice structures, while the intra-strut porosity are the voids arising from process defects were not assessed.

Three levels of porosity (42%, 60% and 72%) were produced for each unit-cell design. These values were selected based on the anticipated Young's moduli based on finite elements analyses (FEA) reported previously [30]. Thus, Young's moduli below 30 GPa were expected for each lattice design, which is compatible with the mechanical properties for

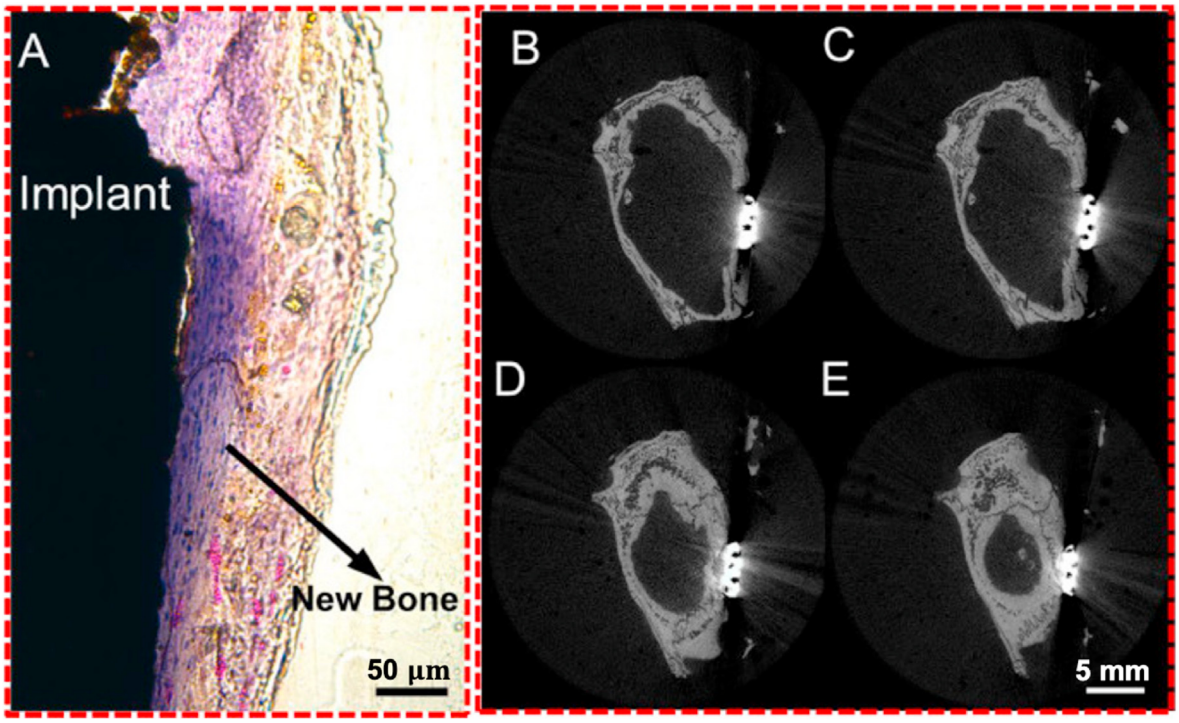

Fig. 1. (A) Histological and (B–E) micro-CT analysis (from bottom (B) to top (E)) showing successful osseointegration of Fe–35Mn scaffold after 4-weeks implantation in rat cranial bone. Scale bar in A: 50 µm. Scale bar in B–E: 5 mm (Reproduced with permission [30]. Copyright 2020, Elsevier).

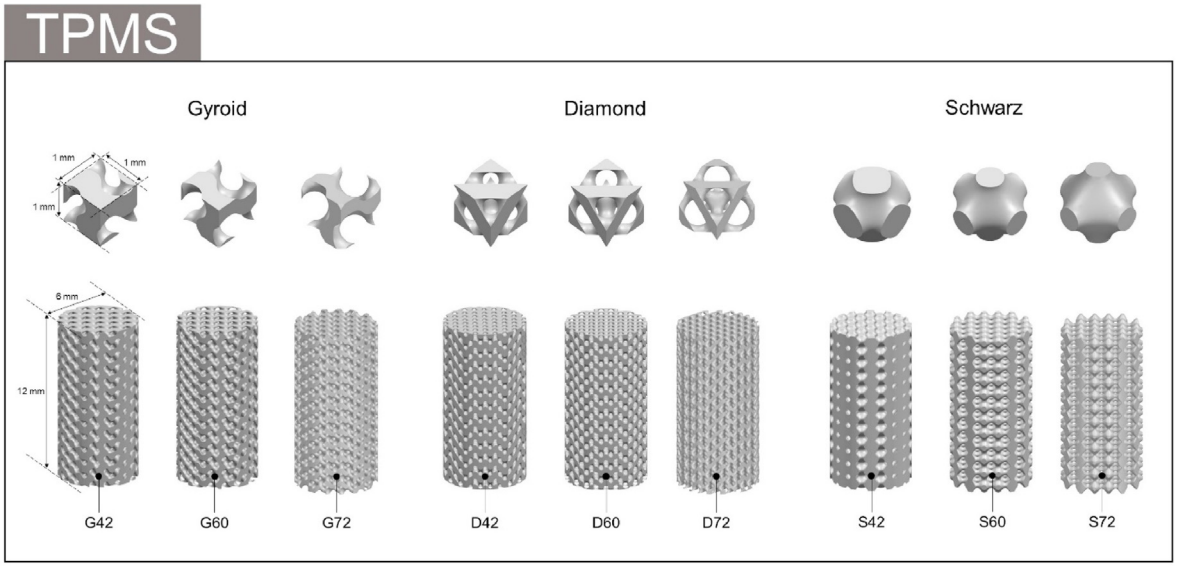

Fig. 2. CAD models of the unit-cell topologies used for the creation of lattices and compression sample designs. All unit-cells and cylindrical samples had identical dimensions to that of the G42 design.

human trabecular and cortical bone. The size of the unit-cell was adjusted to 1 mm^3 (i.e., 1 mm × 1 mm × 1 mm) to provide a suitable pore size for bone tissue applications [40,41]. The resulting pore size and strut size of the scaffolds ranged between 400-1030 µm and 120–480 µm, respectively, depending on the unit-cell design and level of porosity. Further information on morphological characteristics of the scaffold designs is reported in Table 1.

2.2. Selective laser melting (SLM) processing

The cylindrical scaffolds presented in Fig. 2 were produced from a gas atomised spherical Fe–35Mn powder (H.C. Starck Surface Technology and Ceramic Powders GmbH, Goslar, Germany) with the same composition, morphology and particle size distribution (≤44 µm) as used in previous studies [42,43]. The lattices and dense specimens were printed using a Renishaw AM250 Selective Laser Melting (SLM) machine fitted with a reduced build platform system. The nominal beam diameter at the focal plane ($f = 0$ mm) was 75 µm. The SLM processing parameters used for this work and presented in Table 2 are based on previous studies conducted with identical feedstock material [30]. The print was performed under a controlled argon atmosphere with oxygen content below 1000 ppm.

Table 1
Morphological characteristics of CAD models.

Unit-cell type	Sample Reference	K	Designed Porosity (%)	Surface Area to Volume Ratio (mm^{-1})	Min. Strut Thickness (μm)	Max. Pore size[a] (μm)
Gyroid	G42	−0.24	42	5.4	480	400
	G60	0.3	60	7.5	380	500
	G72	0.66	72	10.1	290	610
Diamond	D42	−0.19	42	6.5	400	400
	D60	0.25	60	9.5	300	480
	D72	0.51	72	12.6	230	520
Schwarz primitive	S42	−0.3	42	4.1	240	820
	S60	0.4	60	6.2	140	950
	S72	0.59	72	7.9	120	1030

[a] The maximum pore size was calculated from the diameter of the largest sphere that can fit within a designed lattice pore.

Table 2
SLM processing parameters used for 3D printing of scaffolds.

Parameter	Value
Power, P	125 W
Layer Thickness, z	50 μm
Pulse duration, t_{on}	50 μs
Point distance, d_p	45 μm
Hatch distance, d_h	45 μm
Focal position, f	0 mm

2.3. Microstructure and phase analysis

Electron backscattered diffraction (EBSD) analyses were performed to characterise the phase distributions and texture using a FEI Scios FIB, equipped with EBSD detector. Samples for EBSD were prepared by electropolishing in a solution containing 5% perchloric acid and 95% methanol at −25 °C. All scaffold microstructures were obtained from representative internal lattice locations from the as-built scaffolds.

2.4. Micro-computed tomography scanning

Each fabricated lattice sample type was scanned using a Bruker Skyscan 1272 scanner with the parameters presented in Table 3. Using Fiji software, the reconstructed scans were used to identify morphological differences between the CAD files and the fabricated lattices. Volumes of interest (VOI) of 2 mm^3 were extracted to assess the essential morphological characteristics for the study such as surface areas, volumes and strut/pore sizes.

2.5. Mechanical testing

The lattice specimens were subjected to uniaxial compression testing, according to ISO 13, 314. The test was performed at room temperature using a UTM at a crosshead speed of 2 mm/min. Compressive strain was measured using a video extensometer (Shimadzu AGS-100kNX, Kyoto, Japan). The cylindrical samples were compressed under a continuous load increasing up to 100 kN, or until complete rupture. The compressive strain was measured using an Advanced Video Extensometer (AVE), which tracked two dots on the specimens. Compressive properties such as the compressive modulus (E_c), yield strength at 0.2% offset and compressive strength at 20% strain were determined.

Table 3
Micro-computed tomography scanner settings.

Parameter	Value
Exposure time	7500 ms
Voltage X-ray	100 kV
Current X-ray	100 μA
Rotation step	0.6°
Averaging	2 frames
Energy filter	Cu 0.11 mm
Pixel size (resolution)	7 μm
Image format	1224 x 820

2.6. Static immersion tests

Immersion tests were conducted with the Fe–35Mn scaffolds using modified Hank's balanced salt solution (HBSS, Sigma H1387: 8.0 g NaCl, 0.14 g $CaCl_2$, 0.4 g KCl, 0.35 g $NaHCO_3$, 1.0 g glucose, 0.048 g Na_2HPO_4 (anhydrous), 0.06 g KH_2PO_4 (anhydrous), 0.097 g $MgSO_4$ (anhydrous) dissolved in 1 L deionized water). The HBSS was prepared, followed by temperature and pH adjustments to 37 ± 1 °C and 7.4 ± 0.2, respectively. Before immersion in HBSS, the Fe–35Mn scaffolds were ground with 1200 grit SiC paper to remove the surface oxide and then ultrasonically cleaned in ethanol for 15 min. Post-cleaned scaffolds were subsequently weighed, measured and recorded. The static immersion test was conducted for a duration of 28 days in HBSS at 37 ± 2 °C, following ASTM-G31 [44]. The solution was replaced every 2 days to prevent pH variation beyond 7.4 ± 0.2. After the immersion tests, the surface corrosion products were removed using a commercial rust remover followed by ultrasonic cleaning in ethanol. Scaffolds were weighed after each cleaning round, and the cleaning was repeated until the scaffold weight losses were stable to ensure thorough removal of the corrosion products, as per ASTM G1-03 [45]. The corrosion rate (CR) was calculated according to ASTM G31-72 [44]:

$$CR = 87.4 \times \frac{m_i - m_f}{A \times D \times t} \quad \text{(Eq.4)}$$

where m_i (mg) is the initial weight of scaffolds before immersion, m_f (mg) is the final weight of scaffolds after immersion, A (cm^2) is the exposed area determined by computed tomography (CT), D (g/cm^3) is the alloy density, and t (h) is the immersion time. Corrosion tests results are reported as the mean of three replicates. Appropriate statistical analyses (ANOVA, t-test) were performed to detect differences between the means, and a p value < 0.05 was considered statistically significant.

2.7. Cytocompatibility assessment

Primary human osteoblast cell cultures were established from bone chips collected during extraction of redundant human third molar teeth, as reported in our previous publication [46]. Ethics approval was granted by The University of Queensland human research ethics committee (approval number 2019000134). The cells were cultured in Dulbecco's modified Eagle's alpha-minimum essential medium (α-MEM; Gibco®, Life Technologies Pty Ltd., Australia) containing 10% fetal bovine serum (FBS; In Vitro Technologies, Australia) and 1% (v/v) penicillin/streptomycin (P/S; Gibco®, Life Technologies Pty Ltd., Australia) and incubated at 37 °C in a 95% humidified atmosphere of 5% CO_2. Culture medium was changed every 2–3 days. When the cultured cells reached 90% confluence, they were passaged by a 3-min exposure to 0.25% trypsin (containing 1 mM EDTA, Gibco®, Life Technologies Pty Ltd., Australia).

Cytotoxicity of the Fe–35Mn alloys was evaluated by an indirect cell

assay. Prior to the extraction process, D60 and G60 fabricated scaffolds around 2.0 mm in thickness were rinsed in 100% ethanol for 5 min and dried in an oven overnight. Samples were then sterilized in 70% (v/v) ethanol and kept overnight inside a biosafety cabinet to completely dry. Subsequently, UV light was applied to the samples for 30 min before immersion in α-MEM media. The extraction mediums for both G60 and D60 unit-cells of Fe–35Mn alloy were prepared according to ISO 10993-5 [47]. The alloy samples were immersed in the culture medium according to an extraction ratio of surface area to volume of 1.25 cm^2 per mL in the same culture environment for 72 h. The primary osteoblasts were seeded in a 48-well plate at a density of 3×10^3 cells per well. The culture medium was replaced with fabricated sample extracts of different concentrations (100% and 50%) after culture for 24 h, and then further incubated for 1, 3, and 5 days. The cell viability was assessed by a Live/Dead® assay, as described in previous publications [48,49]. Briefly, the assay was performed after 1, 3 and 5 days from the addition of the extracts onto the cells by staining the cells in the well plate with fluorescein diacetate (FDA-green channel for living cells) or propidium iodide (PI- red channel for dead cells). The well plates were washed twice in PBS, then incubated with FDA (0.8 U/ml) and PI (5 μg/ml) in PBS for 10 min at 37 °C under 5% CO_2. The cells were then rinsed twice in PBS and imaged shortly thereafter using a confocal scanning microscope (Nikon, Eclipse- Ti, U.S.A) at excitation/emission wavelength 488/530 nm for FDA and 561/620 nm for PI.

The effect of extract medium on the metabolic activity and proliferation of the osteoblasts was evaluated by alamarBlue™ and DNA quantification assays, respectively. Cell metabolism was assessed at days 1, 3 and 5 ($n = 6$) assays according to the manufacturer's protocol. Briefly, the culture medium was replaced with 300 μl of medium containing 10% (v/v) alamarBlue solution. The cells were incubated at 37 °C for 4 h. The percentage of reduction was determined using the fluorescence method, and each sample was measured at an excitation wavelength of 560 nm. The emitted fluorescence was collected at a wavelength of 590 nm using a spectrofluorometer (POLARstar Omega, BMG Labtech, Germany). A PicoGreen™ DNA quantification assay (P11496, Invitrogen, Australia) was performed according to the manufacturer's description. On Day 1, 3, and 5, the cultured cells were washed in PBS and frozen at −80 °C until further processing. Subsequently, they were digested overnight at 56 °C in a Tris-EDTA buffered solution containing Proteinase-K (0.5 mg/ml). DNA content was determined using a spectrofluorometer, as described in a previous publication [49].

At selected time points (Day 1 and 5 from adding the extraction media), the cell morphology of the attached cells on the well plates was visualised using 4,6-diamino-2-phenylindole (DAPI, Life Technologies, NY, USA) and Alexa Fluor 568 Phalloidin (Life Technologies, Grand Island, NY, USA). The samples were rinsed in PBS then fixed for 20 min in 4% Paraformaldehyde in PBS. For membrane permeabilization, the samples were incubated for 5 min with 0.5% Triton-X100, rinsed in PBS and incubated for 30 min in a PBS solution having 5 μg/ml DAPI and 0.8 U/ml Alexa Fluor 568 Phalloidin.

2.8. Statistical analysis

For the cell culture data analysis, the data are expressed as mean ± standard deviation. Comparison between groups was assessed by analysis of variance (one-way ANOVA followed by Tukey's test for post hoc analysis). The statistical software Prism 9.0 for windows was used for calculations, and a p value < 0.05 was considered statistically significant.

3. Results and discussion

3.1. Processing and variations in morphological features

All scaffold types could be produced by SLM, excluding the 72% porous diamond structure. This lattice had extensive sections of thin struts requiring very few laser pulses to consolidate, at the limit of the process resolution for SLM under the conditions in this study. As commonly reported for other materials fabricated by SLM, the Fe–35Mn lattices presented some surface irregularities [67–69]. Although small-sized TPMS lattice structures are known for their good processability by additive manufacturing [28], they still present some defects, most notably on downward-facing surfaces. These are mainly caused by the physics of the melt pool and inherent adhesion of powder to the external surfaces (i.e., semi-melted particles). In addition, the areas of overhang that are not supported vertically by prior deposited layers can be subject to severe irregularity due to material warping [50].

Surface irregularities directly contribute to the increase in the surface area to volume ratio (SA:V), as presented in Fig. 3. Each geometry presents a significant increase in SA:V ratio when compared to the CAD equivalent, but a similar trend is observed in the increasing SA:V ratio with increasing porosity for all geometries. The fabricated diamond lattices have the highest variation in SA:V compared to the CAD files. This may be due to its larger solid area and consequently smaller pore size, contributing to greater heat accumulation. This causes an enlarged melt pool and increases powder adhesion leading to higher surface roughness and greater morphological mismatch. Fig. 3b presents a comparison of the minimal strut size between the CAD and CT models. The mismatch is consistent for the gyroid and diamond lattices, with a difference ranging between 53 and 115 μm. However, the fabricated Schwarz lattices presented significantly larger strut sizes compared to the equivalent designed models. Three-dimensional observations of the reconstructed scans indicated that the difference was largely due to increased strut thickness in the z direction where severe sagging due to overhang occurs. The mismatch obtained is in the range of a few powder grains in size.

The SLM processability of the lattice structures is clearly influenced by the unit-cell designs. Factors which contribute to the SLM process resolution include the minimum laser focal area and the powder particle size which influence the size of the melt pool that can form. The gyroid-based scaffolds, which retained the largest minimum strut size across all porosity levels investigated, were the most processable in respects to being able to produce scaffolds with controllable porosity at all porosity levels and which most closely matched to the CAD models. Meanwhile, the Schwarz-based structures tended to show the greatest variation, with the strut thicknesses tending to be substantially larger than the CAD designed models, while the diamond-based scaffolds could not be reliably produced at the highest porosity (72%).

3.2. Mechanical properties

For bone tissue engineering, the essential mechanical characteristics of a scaffold include the compressive Young's modulus, yield strength and ductility. Ideally, the Young's modulus of the fabricated structures should match that of bone to avoid stress shielding [50], and the strength should be superior to ensure that the implant can support physiological loads during healing [51].

The engineering stress-strain curves from the compression tests are presented in Fig. 4, and the extracted mechanical properties are reported in Table 4. For the bulk material, a compressive modulus of 30.1 GPa and a yield strength at 0.2% strain of 460 MPa were measured. These values fall at the upper bound of bone's mechanical properties, i.e., Young's modulus ranging between 1 and 30 GPa and yield strength ranging between 15 and 150 MPa [52,53]. The lattice designs exhibited moduli ranging between 14.7 and 25.1 GPa, 3–11.5 GPa and 1.7–5.4 GPa for the 42%, 60% and 72% porous structures respectively, with the Schwarz geometry having the highest modulus for the three levels of porosity. The superior stiffness observed for the Schwarz geometry can be explained by the alignment of the struts to the loading direction, as previously reported [54]. In contrast, the gyroid and the diamond structures have their struts oriented at 45° to the loading direction, which reduces their resistance to compression and promotes dominant shear and bending loads in contrast to the Schwarz lattice [55].

In respect to strength, the lattices exhibited yield strength at 0.2%

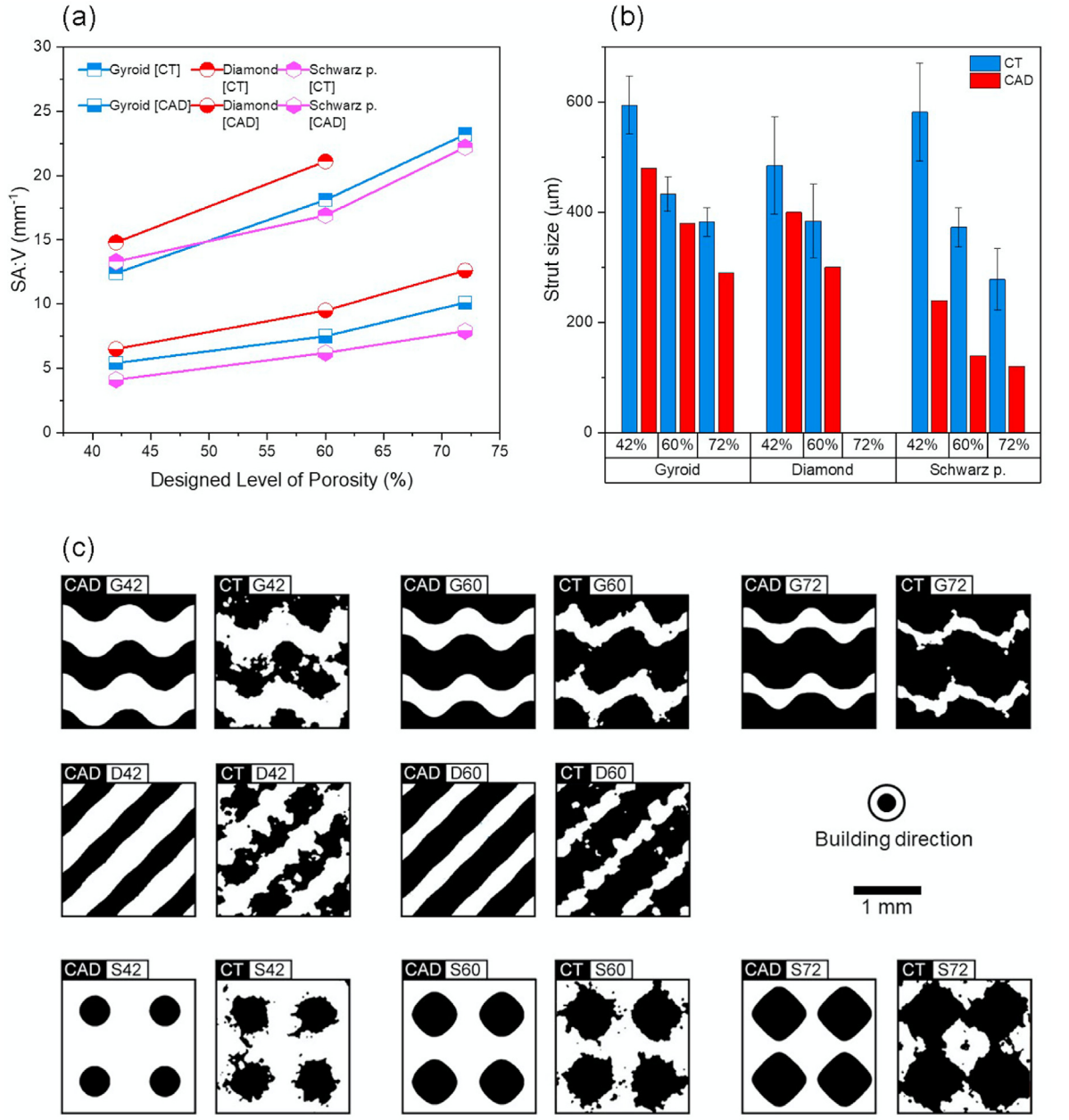

Fig. 3. Differences in morphological features and surface areas between the CAD models and fabricated specimens. (a) Evolution of SA:V ratios with level of porosity (b) Evolution of strut size with level of porosity and (c) Extracted 2D slices showing the discrepancies in morphological features and increased surface areas between CAD models and fabricated specimens from CT scans.

strain ranging between 5 MPa and 77 MPa, which confirms that most of the Fe–35Mn structures presented in this work are sufficiently strong for bone scaffold applications (see relevant mechanical properties of cortical bone in Table 4 [56]). More specifically, the data shows that the gyroid structure was superior to the other two, with a 0.2% offset yield strength of 77 MPa for the 42% porous design and 26 MPa for the 60% porous design. The lowest strength reported was for the diamond lattices, with 16 MPa for the 60% porous specimens. In previous work, the differences in strength between lattice designs for titanium alloy lattices have been attributed to the unit-cell topology primarily, but also to variations in the strut size [57].

In general, all three lattice designs presented high overall ductility with failures typically in the range of 0.3–0.6 strain, except for the S72 sample which exhibited early failure at around 2% strain. Compared to the other designs, the S72 had the thinnest struts of 120 µm which led to compromised strength and structural integrity after small amounts of deformation. The gyroid and diamond structures with lower yield strength than equivalent Schwartz unit cell-based designs, also tended to show a plateau after the yield with only small increases in the stress in response to plastic strain up to around 20–30 % strain, beyond which there were more rapid increases as the lattices further compressed. Meanwhile, the Schwartz type lattices tended to exhibit more constant increases in the stress throughout the applied plastic strain and always maintained higher stresses at equivalent strain levels compared to the other lattice designs, except for in the case of the G42 lattice which exceeded the S42 design at beyond around 30% strain.

The compression test results show that controlling the unit-cell type and porosity allows the lattices to be engineered to achieve mechanical properties suited to specific applications. In general, the Schwartz type lattices were stronger and stiffer than the other unit cell designs. Meanwhile, the diamond and gyroid unit cell-based designs possessed lower strength, were less stiff and were more plastically compliant. For porosity

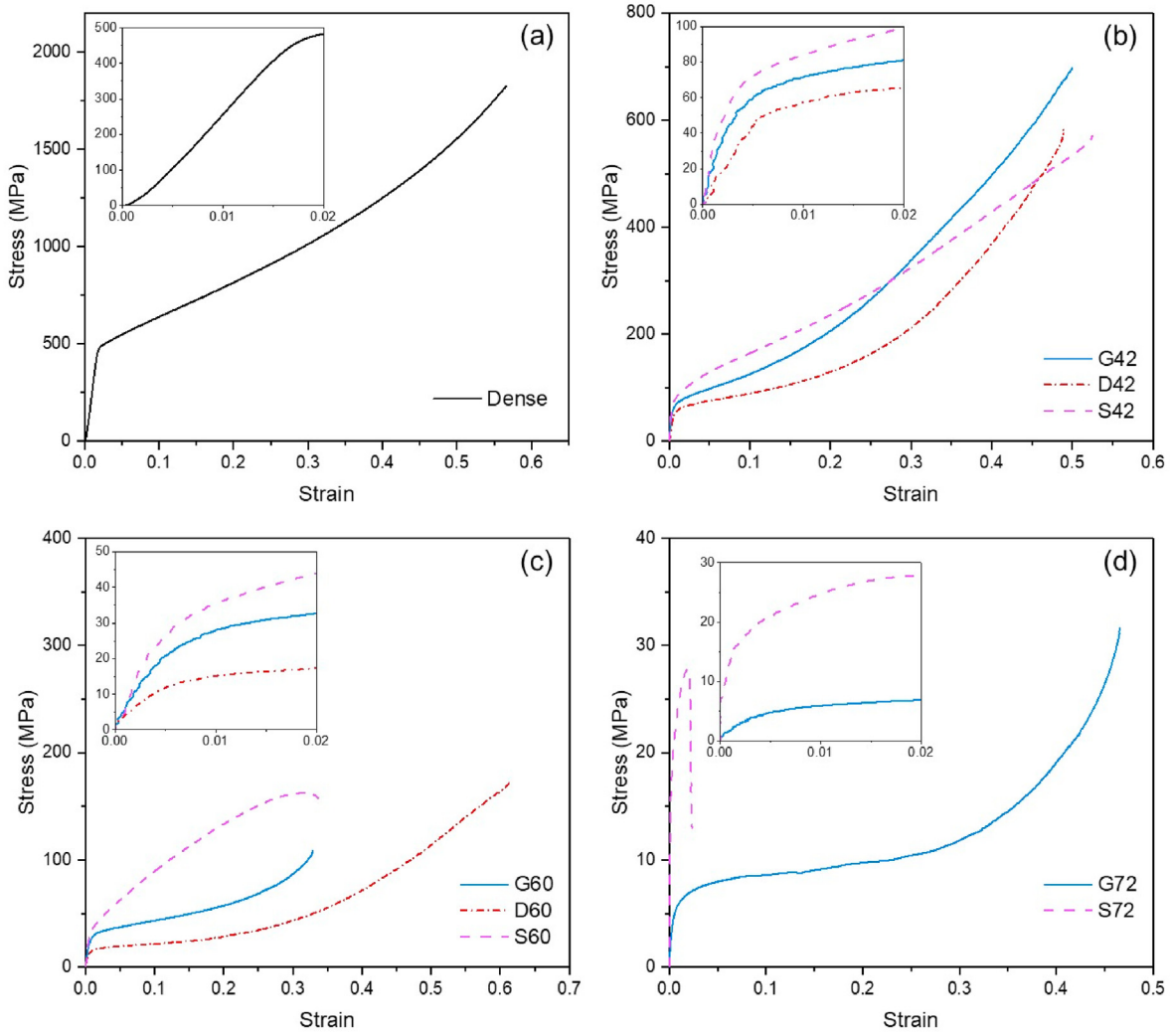

Fig. 4. Engineering stress-strain compression curves for the Fe–35Mn material produced with SLM for (a) dense material (b) 42% porous lattices, (c) 60% porous lattices and (d) 72% porous lattices. Note that the plots are at different scales to ensure better readability.

levels up to 60%, all unit cell designs sustained high strains (>30%) before failure, while the gyroid structure is the only scaffold design which could be manufactured to withstand high levels of plastic strain (>40%) at the higher 72% porosity level.

3.3. Microstructure of lattices

The microstructure in the selective laser melted Fe–Mn lattices were characterised by EBSD analysis. The lattices are of good quality, with only small amounts of intra-strut porosity related to processing defects. The lattices consist of columnar grains aligned along the build direction.

Fig. 5a presents the longitudinal EBSD-inverse pole figure map (EBSD-IPF) and the corresponding pole figures of the bulk Fe–35Mn sample in the as-built condition on its YZ-planes, with the dashed line representing the melt pool boundary. In the EBSD-IPF maps, the red, blue, and green colors display the crystal directions of <001>, <111>, and <101>, respectively. Based on the EBSD results, the major phase of all Fe–35Mn samples in this work is the FCC structured austenitic iron (γ phase), which agrees with XRD results from previous work [30]. From the EBSD-IPF map, the average grain size of the bulk sample is estimated to be ~30.2 μm, with homogenous grain morphology. The corresponding pole figure which is shown inset in Fig. 5b reveals a dominant <110> texture. The misorientation map shown in Fig. 5b from the same region depicted in 5a, reveals that the level of misorientations is weak and typically in the range of ~0.8°–~2.8°.

To further understand the microstructure evolution after the compression tests, the longitudinal EBSD-inverse pole figure (EBSD-IPF) and misorientation map of the compressed bulk Fe–35Mn sample are shown in Fig. 5c. After the compressive deformation, small grains were formed due to the deformation, while the misorientation was only slightly increased. Notably, compared with the as-built sample, the <001> texture was strengthened, which results from grain slipping induced by the compressive deformation.

Microstructures from the as-built Fe–35Mn scaffolds with different unit cell designs are also depicted in Fig. 5c. EBSD-IPF maps for each of the three lattice designs (gyroid, diamond and Schwarz primitive) with varying levels of porosity are shown viewed along and perpendicular to the build direction. The SLM Fe–35Mn lattices exhibit columnar grains which are predominantly aligned to the build direction. Notably, the grains in the Schwarz structures were substantially longer than those in the diamond and gyroid structures, influenced by the cell design and associated porosity distribution. The IPF colors indicate that the texture in different lattice structures differs according to the scaffold design and porosity level. As shown in the pole figures, the Schwarz structure had strong <001> texture. This texture is an influence of scaffold design because the struts of the Schwarz structure are aligned to the build

Table 4
Mechanical properties of Fe–35Mn (dense and lattices) extracted from compression tests. The values presented here are the average (M±SD) of three replicates for each sample type.

Sample reference	Young's Modulus (GPa)	Yield Strength at 0.2% (MPa)	Compressive Strength at 20% strain (MPa)	Strain at failure
Bulk	30.1 ± 0.8	460 ± 8.2	818 ± 4	>0.56
Gyroid 42	14.7 ± 3.8	77 ± 4	212 ± 9	0.45 ± 0.09
Gyroid 60	4.7 ± 0.9	26 ± 2	57 ± 2	0.33 ± 0.02
Gyroid 72	1.7 ± 1.0	5 ± 1	10 ± 5	0.44 ± 0.18
Diamond 42	15.0 ± 6.7	58 ± 4	136 ± 9	0.52 ± 0.04
Diamond 60	3.0 ± 0.7	16 ± 5	32 ± 6	0.58 ± 0.04
Diamond 72	N/A	N/A	N/A	N/A
Schwarz 42	25.1 ± 7.7	64 ± 11	236 ± 2	0.52 ± 0.08
Schwarz 60	11.5 ± 5.2	28 ± 2	124 ± 4	0.28 ± 0.05
Schwarz 72	5.4 ± 1.9	19 ± 2	N/A	0.02 ± 0.01
Human femoral cortical bone (longitudinal) [56]	18.2 ± 1.9	115.06 ± 16.36	205 ± 17.3	1.3 ± 0.3

direction, which promotes grain growth along the build direction due to the heat transfer during SLM processing. In contrast, the diamond structure has a modest <011> texture, while texture in the gyroid lattice structure was relatively weak. This can be understood by considering that the diamond and gyroid scaffold designs, which have struts oriented at 45° to the build direction, limit the growth of columnar grains in the vertical build direction, which in turn lead to greater anisotropy. The results demonstrate the influence of scaffold design on the microstructure of the SLM fabricated Fe–Mn lattices. Moreover, the texture can also be linked to the corrosion behaviours of the SLM fabricated Fe–Mn lattices as corrosion tendencies are generally related to surface energies. This will be discussed in the following section.

Statistical quantitative evaluation of the grain morphologies from the EBSD-IPF maps indicates that porosity and lattice geometry do not have a significant impact on the grain size of the different lattices, with range from ~27 μm to ~29 μm.

3.4. Corrosion results

Fig. 6 shows the average corrosion rates (CRs) of the additively manufactured Fe–35Mn scaffolds after *in vitro* static immersion tests. The CRs are directly influenced by porosity levels, as indicated in Fig. 6a. Consistently, higher degradation rates were observed with increased levels of porosity across all TPMS geometries. For example, the gyroid structure with 42%, 60% and 72% porosity exhibited CRs of 0.11, 0.27, and 0.48 mm year^{-1}, respectively. Regarding the influence of TPMS geometry on CRs, Fig. 6a indicates minimal CR differences between the different lattices at 42% porosity. However, there appears to be greater differences at the higher porosity levels.

Two-way ANOVA results from the CR data of the three geometries at two levels of porosity (42% and 60%) are shown in Table 5. CR results at 70% porosity were not included in the analysis since there is no associated data present for the diamond lattice. The results confirm that both porosity and geometry have significant effects on the CR of the biodegradable lattices, with porosity exhibiting a greater influence than geometry. The ANOVA results also indicate that the interaction of porosity and geometry significantly influences degradation rate. Indeed, this interaction is quite evident when comparing the CR of the lattices with 60% porosity, with the diamond lattice displaying the highest degradation rate due to its significantly elevated SA/V ratio value (more than 40% higher than the other two lattices). Another ANOVA test (3 levels of porosity, 2 geometries) was done to extend the analysis to include the 72% porosity but assessing only the gyroid and Schwarz lattices. Results from this analysis again confirm the significant influence of porosity on CR, but minimal geometry and interaction effects.

The enhanced corrosion performances at increasing porosity can be attributed to the increase in SA:V ratios associated with the TPMS morphological design features, as seen in Fig. 6b. The relationship between corrosion rates and SA:V ratios were explored using three types of models including linear model, quadratic model, and exponential model. The best performed model has been identified as a quadratic model (R^2 = 0.953) described by the equation: y = 0.00041302x2 - 0.00322177x - 0.01372214, where y is the average corrosion rate and x is the structure-specific parameter SA:V. Since corrosion is a surface phenomenon, higher amounts of exposed surface areas enhance the corrosion [58]. The high porosity levels also enhance solution permeability [59], thereby enabling more effective contact between the physiological fluid (Hank's solution) and internal structural features. Similarly, the modest CR differences between the three TPMS geometries for similar porosity levels are directly related to the differences in the SA/V ratios of each lattice (Fig. 6b). Again, it is expected that the higher the SA/V ratio, the higher the resulting CR. This observation is consistent with literature and may be explained by the difference in strut size intrinsic to each design [60]. Finally, though there is no available CR data for the diamond lattice at 72% porosity, it is reasonable to assume that it would have shown the highest CR due to the higher SA/V ratio value inherent to the lattice's design.

The observed trends in CRs are consistent with the conclusions of other studies that large surface areas [61] and reduced strut thickness [13] contribute to accelerate degradation rates. The presence of microstructural texture may also contribute to the enhanced corrosion rate of the diamond lattice. The EBSD results detected a <011> texture in the 3D-printed diamond Fe–Mn scaffolds compared with the <001> texture observed in the Schwarz structures at similar porosity levels. It is possible that the <011> plane of the face-centred cubic (FCC) austenite structure (Fe–Mn alloys in this study), by having a higher planar density, is more chemically active than the <001> plane, resulting in higher tendency to corrode [62].

3.5. In vitro cell culture

In vitro cell responses to the D60 and G60 extracts were assessed using primary osteoblast cells after 1, 3 and 5 days. The cytotoxicity of the D60 and G60 fabricated scaffolds on osteoblasts was assessed at the various time points by a live/dead assay with 100% and 50% extracts, and the results are shown in Fig. 7(a and b). Based on the analysis of confocal images (Fig. 7a), no significant differences were observed between the groups at each time point. However, when examining the quantitative data presented in Fig. 7b, it is evident that on day 1, the 3D printed samples, with the exception of D60 at 50% extraction, exhibited a lower percentage of reduction when compared to the negative control. As the culture time extended, the printed scaffolds displayed no signs of cytotoxicity at the tested concentrations across all three time points, indicating excellent cytocompatibility of the scaffolds. The cell metabolic activity was measured by alamarBlue (Fig. 8a) and this demonstrated a similar trend to the DNA quantification data (Fig. 8b), with minimal differences between the culture media (negative control) and extracts at high (100%) and low (50%) concentrations. The effect of the extracts on cell morphology was assessed on D60 scaffold by confocal laser microscopy (Fig. 8c) (there was no difference between the groups, data not shown). It was observed that the cells maintained confluence and a normal morphology from day 1, indicating that the extracts do not have a negative influence on the cells. Indeed, the presence of Fe and Mn ions in the extracts did not diminish cell viability, consistent with previous reports [2]. Iron is an essential element in the human body and has been

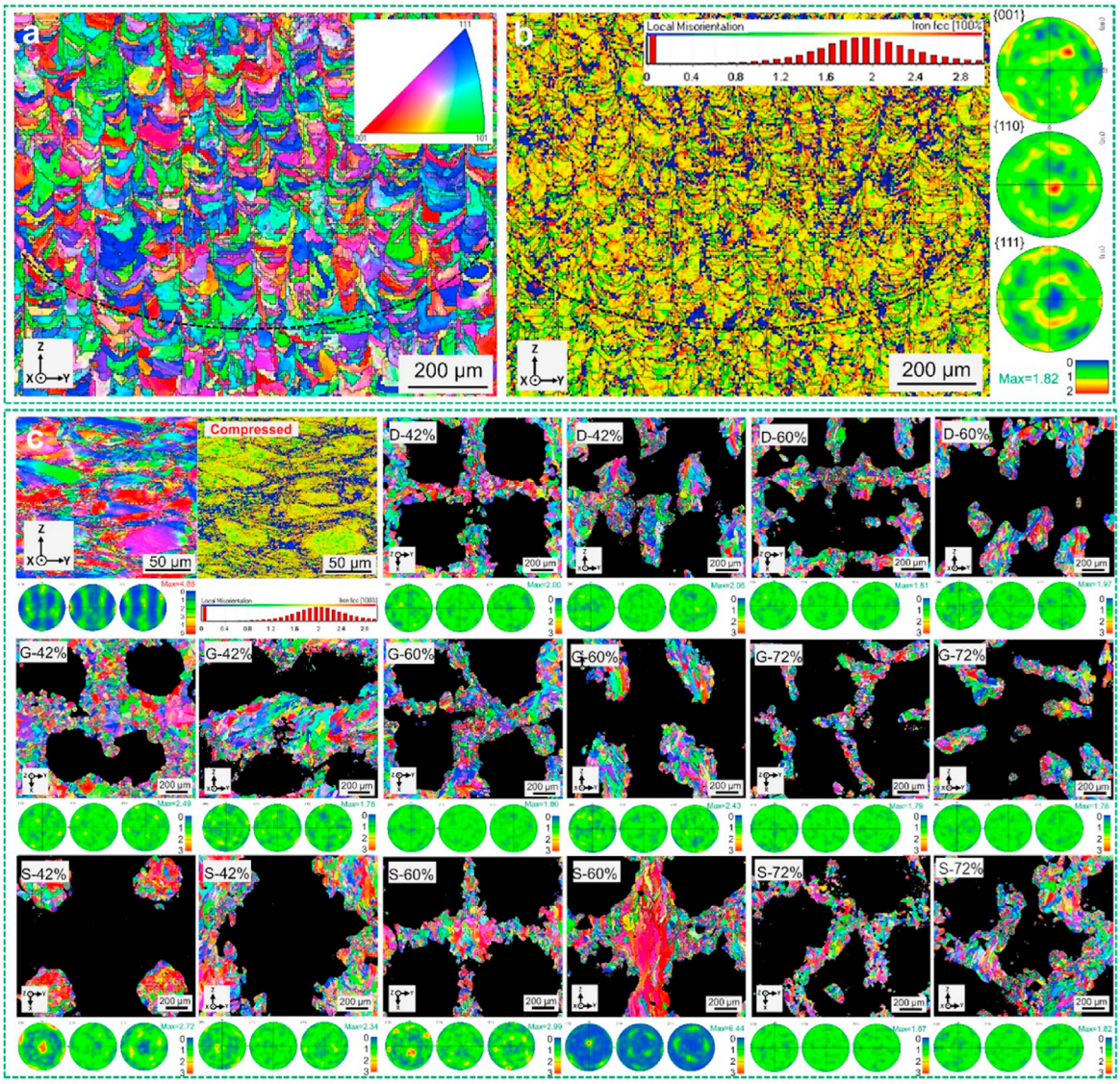

Fig. 5. (a) Longitudinal EBSD-inverse pole figure (EBSD-IPF) and (b) corresponding misorientation map and pole figures of the bulk sample, (c) Longitudinal EBSD map and corresponding misorientation map and pole figures of the bulk sample after the compression test; EBSD maps and corresponding {001}, {110} and {111} pole figures of the three lattice structures (gyroid, diamond and Schwarz primitive) with different porosity designs, viewed along and perpendicular to the building direction (Z-axis), respectively.

demonstrated to have a high threshold for toxicity to occur, i.e., 350–500 μg dl^{-}1 in serum. Extracellular iron exclusively binds to transferrin, which maintains iron-solubility and restricts exposure to lower, non-toxic levels [63]. Although Mn shows a potential to be toxic to human cells, i.e., Mn^{3+} at a level of 3–5.6 μg dl^{-}1 can cause neurologic symptoms, its cytotoxic properties are alleviated when combined with Fe in the Fe–35Mn alloy to form a homogeneous solid solution of the γ phase [2]. Indeed, the Fe–35Mn alloy possesses very different characteristics than its forming elements (Fe^{2+}, and Mn^{3+}), demonstrating a far more favourable influence on cell function, with our findings being consistent with previously reported cell culture work on Fe–35Mn alloys [2].

Our preliminary *in vitro* culture work demonstrated the promising cytocompatibility properties of the fabricated scaffolds. Further studies using both indirect and direct cell culture assays to assess various cell functions, including adhesion, migration and differentiation, will greatly increase insight into the cellular effects of the Fe–35Mn alloys.

4. Conclusions

In this study, lattices based on different TPMS designs were fabricated via selective laser melting of a Fe–35Mn alloy and the mechanical properties, degradation behaviours and cytocompatibility were assessed. Important conclusions from the study are:

(i) The lattice designs exhibited moduli ranging between 14.7 and 25.1 GPa, 3–11.5 GPa and 1.7–5.4 GPa for the 42%, 60% and 72% porous structures, respectively. The superior stiffness observed for the Schwarz geometry is due to the alignment of the struts to the loading direction. In contrast, the gyroid and the diamond structures have struts oriented at 45° to the loading direction which reduces the compressive stiffness and promotes dominant shear and bending deformation.

(ii) The different lattice designs exhibited 0.2% offset yield strengths between 5 MPa and 77 MPa, confirming their suitability for cortical bone scaffold applications. More specifically, the data shows that the gyroid structure was superior to the diamond and

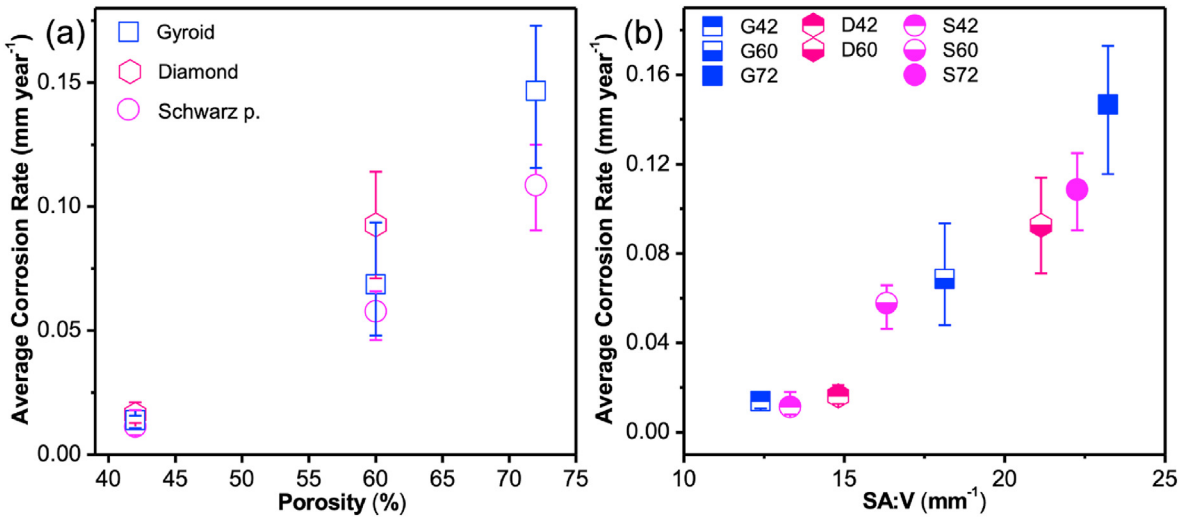

Fig. 6. The average corrosion rates of the different TPMS Fe–35Mn scaffolds plotted as a function of (a) level of porosity and (b) surface area/volume after the static immersion test.

Table 5
Two-way ANOVA ($p < 0.05$) results showing the significant influence of porosity (42% and 60%), geometry (diamond, gyroid and Schwarz), and their interaction on the corrosion rate of the lattice (taken at porosity levels 42 and 60%).

Source of Variation	SS	df	MS	F	P-value	F crit
Porosity	0.128	1	0.128	168.4	2.01E-08	4.74
Geometry	0.013	2	0.006	8.2	0.005713	3.89
Interaction	0.024	2	0.012	15.9	0.000422	3.89
Within	0.009	12	0.001			
Total	0.174	17				

SS = sum of squares; df = degrees of freedom; MS = mean square; F=F ratio.

Schwarz lattices, with a yield strength of 77 MPa for the 42% porous design and 26 MPa for the 60% porous design. However, at 72% porosity the lowest strength of 5 MPa was obtained for the gyroid lattice.

(iii) Degradation rates significantly increased with increasing porosity (42%, 60%, 72%) for the three investigated TPMS geometries. Lattice geometry and porosity had a moderate impact on CR. The positive influence of porosity and geometry on CR is directly related to the increase in surface area-to-volume ratio (SA/V). The observed dependence of corrosion rate on these factors provides a pathway to design biodegradable porous implants with tunable degradation behaviours.

(iv) Assessments of the effect of low (50%) and high (100%) concentration extracts on human osteoblast viability, metabolic activity and DNA content did not show any adverse effects, demonstrating the biocompatibility of the SLM fabricated Fe–35Mn alloy.

This study has shown that TPMS based lattice implant designs produced from a biodegradable Fe–35Mn alloy offer excellent biocompatibility with the ability to tailor the mechanical properties and degradation rates to specific clinical applications. The results of this work provide a feasible solution to develop tuneable biodegradable implants for hard tissue engineering using TPMS designs. Meanwhile, additive manufacturing has demonstrated its ability to achieve accurate and efficient fabrication of intricate lattice structures. This capability positions additive manufacturing as a driving force behind the evolution of medical device design, promoting the timely delivery of high-quality medical implants to patients with personalised performances for improved tissue regeneration.

Despite of the findings, the relationships between TPMS structures and implant's mechanical and corrosion performances still need to be fully understood. New insights might be obtained by considering the microstructural defects generated during the additive manufacturing

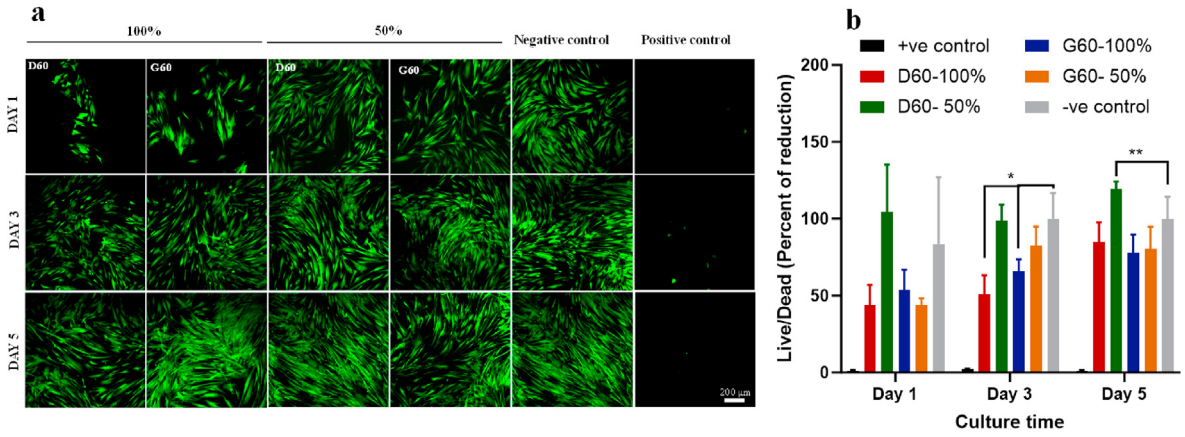

Fig. 7. Live/dead cells assay of indirect extraction cell culture method at 100% and 50% extraction, (2) confocal images and (b) percent of reduction as a function of negative control. The culture medium was used as negative control and culture medium with 10% dimethyl sulfoxide as positive control. * = $p < 0.05$ and ** = $p < 0.01$.

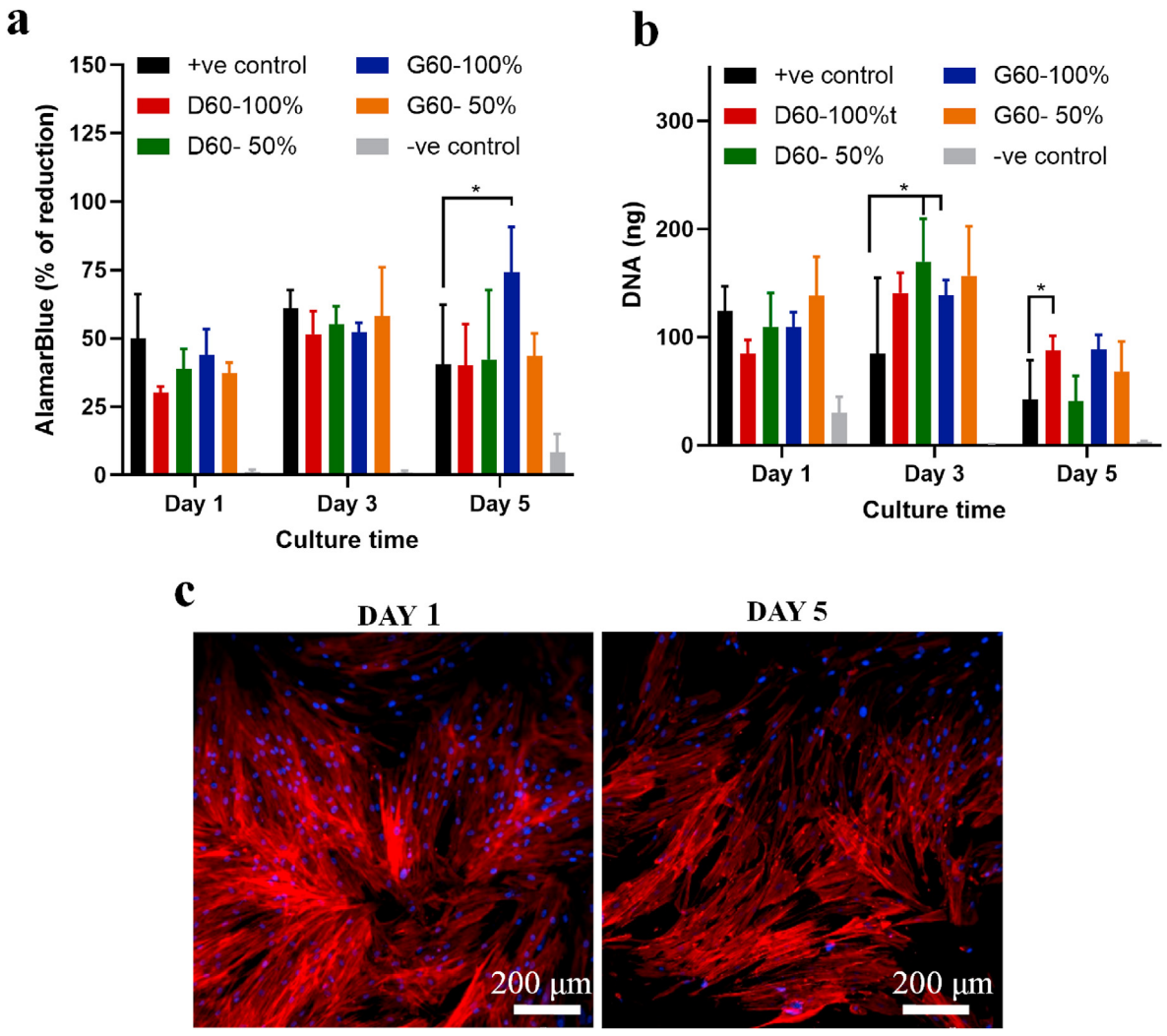

Fig. 8. (a) Metabolic activity as measured by Aalamar Blue; (b) proliferation as assessed by PicoGreen DNA quantification assay (DNA content was measured and normalised by the DNA content of the initial seeding solution) of osteoblasts cells after 1, 3 and 5 days of culture using indirect extraction from D60 and G60 fabricated scaffolds. (c) DAPI (blue)/Phalloidin (read) staining of D60 after day 1 and day 5 of replacing the culture media with the extracted solution. For statistical analysis, each group is compared to + ve control group, * = $p < 0.05$.

process. The effects of other TPMS designs such as the lidinoid minimal surface and other additive manufacturing methods on implant's performances also deserve to be further investigated.

In terms of the biocompatibility, although a good cytocompatibility to primary human osteoblasts cells was observed *in vitro*, the *in vivo* osteoimmunity responses of these scaffolds still need to be investigated to expedite their clinical translation towards bone regeneration. Developing composite scaffold materials [64] may provide a promising solution to regulate the osteoimmunity responses for augmented bone regeneration. For example, a composite scaffold material composed of deferoxamine@poly(ε-caprolactone) nanoparticles, manganese carbonyl nanosheets, gelatin methacryloyl hydrogel, and a polylactide/hydroxyapatite (HA) matrix has been reported to augment bone repair by facilitating the balance of the immune system and bone metabolism [65–69].

CRediT authorship contribution statement

Matthew S. Dargusch: Conceptualization, Methodology, Supervision, Funding acquisition, Writing – original draft, Writing – review & editing. **Nicolas Soro:** Formal analysis, Data curation. **Ali Gokhan Demir:** Methodology, Investigation, Formal analysis. **Jeffrey Venezuela:** Formal analysis, Writing – review & editing. **Qiang Sun:** Investigation. **Yuan Wang:** Investigation, Visualization, Writing – original draft, Writing – review & editing. **Abdalla Abdal-hay:** Investigation, Methodology, Writing – review & editing. **Aya Q. Alali:** Investigation. **Saso Ivanovski:** Investigation, Writing – review & editing. **Barbara Previtali:** Methodology, Investigation. **Damon Kent:** Investigation, Writing – review & editing.

Declaration of competing interest

The authors declare that they have no known competing financial interests or personal relationships that could have appeared to influence the work reported in this paper.

Acknowledgments

The authors acknowledge the support of the Australian Research Council through the ARC Research Hub for Advanced Manufacturing of Medical Devices (IH150100024). The authors would also like to acknowledge the Translational Research Institute (TRI), the core facilities that enable this research and the technical support provided by Kamil Sokolowski. The Skyscan 1272 µCT used in this research was purchased by the Mater Foundation using funds donated by the Lions Club of Australia. The Italian Ministry of Education, University and Research is acknowledged for the support provided through the Project

“Department of Excellence LIS4.0 - Lightweight and Smart Structures for Industry 4.0”.

References

[1] S.M. Perren, Evolution of the internal fixation of long bone fractures, J. Bone Joint Surg. 84-B (2002) 1093–1110.
[2] H. Hermawan, A. Purnama, D. Dube, J. Couet, D. Mantovani, Fe–Mn alloys for metallic biodegradable stents: degradation and cell viability studies, Acta Biomater. 6 (2010) 1852–1860.
[3] M. Prakasam, J. Locs, K. Salma-Ancane, D. Loca, A. Largeteau, L. Berzina-Cimdina, Biodegradable materials and metallic implants-A review, J. Funct. Biomater. 8 (2017).
[4] H.-S. Han, S. Loffredo, I. Jun, J. Edwards, Y.-C. Kim, H.-K. Seok, F. Witte, D. Mantovani, S. Glyn-Jones, Current status and outlook on the clinical translation of biodegradable metals, Mater. Today 23 (2019) 57–71.
[5] J. Venezuela, M.S. Dargusch, Addressing the slow corrosion rate of biodegradable Fe-Mn: current approaches and future trends, Curr. Opin. Solid State Mater. Sci. 24 (2020).
[6] F. Witte, The history of biodegradable magnesium implants: a review, Acta Biomater. 6 (2010) 1680–1692.
[7] A. Abdal-hay, N.A. Barakat, J.K. Lim, Hydroxyapatite-doped poly (lactic acid) porous film coating for enhanced bioactivity and corrosion behavior of AZ31 Mg alloy for orthopedic applications, Ceram. Int. 39 (2013) 183–195.
[8] J. Venezuela, M.S. Dargusch, The influence of alloying and fabrication techniques on the mechanical properties, biodegradability and biocompatibility of zinc: a comprehensive review, Acta Biomater. 87 (2019) 1–40.
[9] H. Hermawan, D. Dube, D. Mantovani, Degradable metallic biomaterials: design and development of Fe-Mn alloys for stents, J. Biomed. Mater. Res. 93 (2010) 1–11.
[10] K.H. Lim, L.J. Riddell, C.A. Nowson, A.O. Booth, E.A. Szymlek-Gay, Iron and zinc nutrition in the economically-developed world: a review, Nutrients 5 (2013) 3184–3211.
[11] E. Zhang, H. Chen, F. Shen, Biocorrosion properties and blood and cell compatibility of pure iron as a biodegradable biomaterial, J. Mater. Sci. Mater. Med. 21 (2010) 2151–2163.
[12] M. Schinhammer, A.C. Hanzi, J.F. Loffler, P.J. Uggowitzer, Design strategy for biodegradable Fe-based alloys for medical applications, Acta Biomater. 6 (2010) 1705–1713.
[13] M. Peuster, C. Hesse, T. Schloo, C. Fink, P. Beerbaum, C. von Schnakenburg, Long-term biocompatibility of a corrodible peripheral iron stent in the porcine descending aorta, Biomaterials 27 (2006) 4955–4962.
[14] M.S. Dargusch, J. Venezuela, A. Dehghan-Manshadi, S. Johnston, N. Yang, K. Mardon, et al., In vivo evaluation of bioabsorbable Fe-35Mn-1Ag: first reports on in vivo hydrogen gas evolution in Fe-based implants, Adv. Healthcare Mater. (2020) e2000667.
[15] T. Kraus, F. Moszner, S. Fischerauer, M. Fiedler, E. Martinelli, J. Eichler, et al., Biodegradable Fe-based alloys for use in osteosynthesis: outcome of an in vivo study after 52weeks, Acta Biomater. 10 (2014) 3346–3353.
[16] H. Hermawan, H. Alamdari, D. Mantovani, D. Dubé, Iron–manganese: new class of metallic degradable biomaterials prepared by powder metallurgy, Powder Metall. 51 (2008) 38–45.
[17] M.S. Dargusch, A. Dehghan-Manshadi, M. Shahbazi, J. Venezuela, X. Tran, J. Song, et al., Exploring the role of manganese on the microstructure, mechanical properties, biodegradability, and biocompatibility of porous iron-based scaffolds, ACS Biomater. Sci. Eng. 5 (2019) 1686–1702.
[18] M. Kupková, M. Hrubovčáková, M. Kupka, R. Oriňáková, A.M. Turoňová, Sintering behaviour, graded microstructure and corrosion performance of sintered Fe-Mn biomaterials, Int. J. Electrochem. Sci. 10 (2015) 9256–9268.
[19] B. Liu, Y.F. Zheng, Effects of alloying elements (Mn, Co, Al, W, Sn, B, C and S) on biodegradability and in vitro biocompatibility of pure iron, Acta Biomater. 7 (2011) 1407–1420.
[20] Y. Li, H. Jahr, J. Zhou, A.A. Zadpoor, Additively manufactured biodegradable porous metals, Acta Biomater. 115 (2020) 29–50.
[21] M. Heiden, E. Nauman, L. Stanciu, Bioresorbable Fe-Mn and Fe-Mn-HA materials for orthopedic implantation: enhancing degradation through porosity control, Adv. Healthcare Mater. 6 (2017).
[22] G. Ryan, A. Pandit, D.P. Apatsidis, Fabrication methods of porous metals for use in orthopaedic applications, Biomaterials 27 (2006) 2651–2670.
[23] D.A. Shimko, V.F. Shimko, E.A. Sander, K.F. Dickson, E.A. Nauman, Effect of porosity on the fluid flow characteristics and mechanical properties of tantalum scaffolds, J. Biomed. Mater. Res. B Appl. Biomater. 73B (2005) 315–324.
[24] N. Soro, L. Brassart, Y. Chen, M. Veidt, H. Attar, M.S. Dargusch, Finite element analysis of porous commercially pure titanium for biomedical implant application, Mater. Sci. Eng., A 725 (2018) 43–50.
[25] N. Soro, H. Attar, X. Wu, M.S. Dargusch, Investigation of the structure and mechanical properties of additively manufactured Ti-6Al-4V biomedical scaffolds designed with a Schwartz primitive unit-cell, Mater. Sci. Eng., A 745 (2019) 195–202.
[26] M. Afshar, A.P. Anaraki, H. Montazerian, J. Kadkhodapour, Additive manufacturing and mechanical characterization of graded porosity scaffolds designed based on triply periodic minimal surface architectures, J. Mech. Behav. Biomed. Mater. 62 (2016) 481–494.
[27] S.C. Kapfer, S.T. Hyde, K. Mecke, C.H. Arns, G.E. Schröder-Turk, Minimal surface scaffold designs for tissue engineering, Biomaterials 32 (2011) 6875–6882.
[28] L. Yuan, S. Ding, C. Wen, Additive manufacturing technology for porous metal implant applications and triple minimal surface structures: a review, Bioact. Mater. 4 (2019) 56–70.
[29] C. Yan, L. Hao, A. Hussein, P. Young, Ti-6Al-4V triply periodic minimal surface structures for bone implants fabricated via selective laser melting, J. Mech. Behav. Biomed. Mater. 51 (2015) 61–73.
[30] D. Carluccio, C. Xu, J. Venezuela, Y. Cao, D. Kent, M. Bermingham, et al., Additively manufactured iron-manganese for biodegradable porous load-bearing bone scaffold application, Acta Biomater. 103 (2020) 346–360.
[31] A. Ataee, Y. Li, D. Fraser, G. Song, C. Wen, Anisotropic Ti-6Al-4V gyroid scaffolds manufactured by electron beam melting (EBM) for bone implant applications, Mater. Des. 137 (2018) 345–354.
[32] C. Yan, L. Hao, A. Hussein, P. Young, Ti–6Al–4V triply periodic minimal surface structures for bone implants fabricated via selective laser melting, J. Mech. Behav. Biomed. Mater. 51 (2015) 61–73.
[33] F. Liu, Z. Mao, P. Zhang, D.Z. Zhang, J. Jiang, Z. Ma, Functionally graded porous scaffolds in multiple patterns: new design method, physical and mechanical properties, Mater. Des. 160 (2018) 849–860.
[34] A.A. Zadpoor, Bone tissue regeneration: the role of scaffold geometry, Biomater. Sci. 3 (2015) 231–245.
[35] M. Speirs, B. Van Hooreweder, J. Van Humbeeck, J.P. Kruth, Fatigue behaviour of NiTi shape memory alloy scaffolds produced by SLM, a unit cell design comparison, J. Mech. Behav. Biomed. Mater. 70 (2017) 53–59.
[36] T. Femmer, A.J.C. Kuehne, M. Wessling, Estimation of the structure dependent performance of 3-D rapid prototyped membranes, Chem. Eng. J. 273 (2015) 438–445.
[37] D. Barba, E. Alabort, R. Reed, Synthetic bone: design by additive manufacturing, Acta Biomater. 97 (2019) 637–656.
[38] M.M. Sychov, L.A. Lebedev, S.V. Dyachenko, L.A. Nefedova, Mechanical properties of energy-absorbing structures with triply periodic minimal surface topology, Acta Astronaut. 150 (2018) 81–84.
[39] I. Maskery, L. Sturm, A.O. Aremu, A. Panesar, C.B. Williams, C.J. Tuck, R.D. Wildman, I.A. Ashcroft, R.J.M. Hague, Insights into the mechanical properties of several triply periodic minimal surface lattice structures made by polymer additive manufacturing, Polymer 152 (2018) 62–71.
[40] D. Hara, Y. Nakashima, T. Sato, M. Hirata, M. Kanazawa, Y. Kohno, et al., Bone bonding strength of diamond-structured porous titanium-alloy implants manufactured using the electron beam-melting technique, Mater. Sci. Eng. C 59 (2016) 1047–1052.
[41] L.G. Sicchieri, G.E. Crippa, P.T. de Oliveira, M.M. Beloti, A.L. Rosa, Pore size regulates cell and tissue interactions with PLGA–CaP scaffolds used for bone engineering, Journal of tissue engineering and regenerative medicine 6 (2012) 155–162.
[42] D. Carluccio, A.G. Demir, L. Caprio, B. Previtali, M.J. Bermingham, M.S. Dargusch, The influence of laser processing parameters on the densification and surface morphology of pure Fe and Fe-35Mn scaffolds produced by selective laser melting, J. Manuf. Process. 40 (2019) 113–121.
[43] D. Carluccio, M. Bermingham, M.S. Dargusch, A.G. Demir, L. Caprio, B. Previtali, Selective laser melting Fe and Fe-35Mn for biodegradable implants, Int. J. Mod. Phys. B 34 (2020) 1–6.
[44] ASTM, ASTM G31-72 Standard Practice for Laboratory Immersion Corrosion Testing of Metals, ASTM International, West Conshohocken, PA, 2004.
[45] ASTM, ASTM G1-03 Standard Practice for Preparing, Cleaning, and Evaluating Corrosion Test Specimens, ASTM International, West Conshohocken, PA, 2017.
[46] H. Haase, S. Ivanovski, M. Waters, P. Bartold, Growth hormone regulates osteogenic marker mRNA expression in human periodontal fibroblasts and alveolar bone-derived cells, J. Periodontal. Res. 38 (2003) 366–374.
[47] I. Iso, 10993–5: 2009 Biological Evaluation of Medical Devices—Part 5: Tests for in Vitro Cytotoxicity, International Organization for Standardization, Geneva, 2009.
[48] M.G. Ali, H.M. Mousa, F. Blaudez, M. Abd El-sadek, M. Mohamed, G. Abdel-Jaber, et al., Dual nanofiber scaffolds composed of polyurethane-gelatin/nylon 6-gelatin for bone tissue engineering, Colloids Surf. A Physicochem. Eng. Asp. 597 (2020) 124817.
[49] A. Abdal-hay, N.T. Raveendran, B. Fournier, S. Ivanovski, Fabrication of biocompatible and bioabsorbable polycaprolactone/magnesium hydroxide 3D printed scaffolds: degradation and in vitro osteoblasts interactions, Compos. B Eng. 197 (2020) 108158.
[50] V. Finazzi, A.G. Demir, C.A. Biffi, C. Chiastra, F. Migliavacca, L. Petrini, et al., Design rules for producing cardiovascular stents by selective laser melting: geometrical constraints and opportunities, Procedia Struct. Integr. 15 (2019) 16–23.
[51] M. Geetha, A.K. Singh, R. Asokamani, A.K. Gogia, Ti based biomaterials, the ultimate choice for orthopaedic implants–a review, Prog. Mater. Sci. 54 (2009) 397–425.
[52] Y.N. Yeni, D.P. Fyhrie, A rate-dependent microcrack-bridging model that can explain the strain rate dependency of cortical bone apparent yield strength, J. Biomech. 36 (2003) 1343–1353.
[53] K. Athanasiou, C.-F. Zhu, D. Lanctot, C. Agrawal, X. Wang, Fundamentals of biomechanics in tissue engineering of bone, Tissue Eng. 6 (2000) 361–381.
[54] S. Limmahakhun, A. Oloyede, K. Sitthiseripratip, Y. Xiao, C. Yan, 3D-printed cellular structures for bone biomimetic implants, Addit. Manuf. 15 (2017) 93–101.
[55] N. Soro, N. Saintier, J. Merzeau, M. Veidt, M.S. Dargusch, Quasi-static and fatigue properties of graded Ti-6Al-4V lattices produced by Laser Powder Bed Fusion (LPBF), Addit. Manuf. (2020) 101653.
[56] E.F. Morgan, G.U. Unnikrisnan, A.I. Hussein, Bone mechanical properties in healthy and diseased states, Annu. Rev. Biomed. Eng. 20 (2018) 119–143.

[57] C. Han, C. Yan, S. Wen, T. Xu, S. Li, J. Liu, et al., Effects of the unit cell topology on the compression properties of porous Co-Cr scaffolds fabricated via selective laser melting, Rapid Prototyp. J. (2017).
[58] A.H. Yusop, A.A. Bakir, N.A. Shaharom, M.R. Abdul Kadir, H. Hermawan, Porous biodegradable metals for hard tissue scaffolds: a review, International Journal of Biomaterials 2012 (2012) 641430.
[59] S. Ma, Q. Tang, X. Han, Q. Feng, J. Song, R. Setchi, et al., Manufacturability, Mechanical Properties, Mass-Transport Properties and Biocompatibility of Triply Periodic Minimal Surface (TPMS) Porous Scaffolds Fabricated by Selective Laser Melting, Materials & Design, 2020, p. 195.
[60] A. Du Plessis, I. Yadroitsava, I. Yadroitsev, S.G. Le Roux, D.C. Blaine, Numerical comparison of lattice unit cell designs for medical implants by additive manufacturing, Virtual Phys. Prototyp. 13 (2018) 266–281.
[61] M. Hočevar, Č. Donik, I. Paulin, A. Kocijan, F. Tehovnik, J. Burja, et al., Corrosion on polished and laser-textured surfaces of an Fe–Mn biodegradable alloy, Materiali in tehnologije 51 (2017) 1037–1041.
[62] S. Dong, X. Chen, E.C. La Plante, M. Gussev, K. Leonard, G. Sant, Elucidating the Grain-Orientation Dependent Corrosion Rates of Austenitic Stainless Steels, Materials & Design, 2020, p. 191.
[63] G. Papanikolaou, K. Pantopoulos, Iron metabolism and toxicity, Toxicol. Appl. Pharmacol. 202 (2005) 199–211.
[64] D. Zhao, T. Zhu, J. Li, Li Cui, Z. Zhang, X. Zhuang, J. Ding, Poly(lactic-co-glycolic acid)-based composite bone-substitute materials, Bioact. Mater. 6 (2021) 346–360.
[65] Z. Liu, J. Zhang, C. Fu, J. Ding, Osteoimmunity-regulating biomaterials promote bone regeneration, Asian J. Pharm. Sci. 18 (2023) 100774.
[66] J. Zhang, D. Tong, H. Song, R. Ruan, Y. Sun, Y. Lin, J. Wang, L. Hou, J. Dai, J. Ding, H. Yang, Osteoimmunity-Regulating biomimetically hierarchical scaffold for augmented bone regeneration, Adv. Mater. 34 (2022) 2202044.
[67] C. Li, D. Liu, G. Liu, S. Liu, X. Jin, Y. Bai, Surface characteristics enhancement and morphology evolution of selective-laser-melting (SLM) fabricated stainless steel 316L by laser polishing, Opt Laser. Technol. 162 (2023) 109246.
[68] D. Carluccio, A.G. Demir, L. Caprio, B. Previtali, M.J. Bermingham, M.S. Dargusch, The influence of laser processing parameters on the densification and surface morphology of pure Fe and Fe-35Mn scaffolds produced by selective laser melting, J. Manuf. Process. 40 (2019) 113–121.
[69] A. Dehghan-Manshadi, J. Venezuela, A.G. Demir, Q. Ye, M.S. Dargusch, Additively manufactured Fe-35Mn-1Ag lattice structures for biomedical applications, J. Manuf. Process. 80 (2022) 642–650.